

Available online at [www.sciencedirect.com](http://www.sciencedirect.com)

**jmr&t**  
Journal of Materials Research and Technology

journal homepage: [www.elsevier.com/locate/jmrt](http://www.elsevier.com/locate/jmrt)**Original Article****A facile strategy for one-step hydrothermal preparation of porous hydroxyapatite microspheres with core–shell structure**

Wei-li Xu <sup>a,b,c</sup>, Bing Liu <sup>a,b,c,d</sup>, Yin-chuan Wang <sup>a,b,c</sup>, Gui-yong Xiao <sup>a,b,c</sup>,  
Xin Chen <sup>a,b,c</sup>, Wen-hua Xu <sup>a,b,c</sup>, Yu-peng Lu <sup>a,b,c,\*</sup>

<sup>a</sup> Key Laboratory for Liquid-Solid Structural Evolution and Processing of Materials, Ministry of Education, Shandong University, Ji'nan, China

<sup>b</sup> School of Materials Science and Engineering, Shandong University, Ji'nan, China

<sup>c</sup> Suzhou Institute of Shandong University, Suzhou, China

<sup>d</sup> School of Stomatology, Shandong First Medical University & Shandong Academy of Medical Sciences, Ji'nan, China

**ARTICLE INFO****Article history:**

Received 3 November 2021

Accepted 1 January 2022

Available online 6 January 2022

**Keywords:**

Hydroxyapatite

Core-shell

Microsphere

One-step

Sodium trimetaphosphate

**ABSTRACT**

Core-shell microspheres have attracted widespread attention in the field of drug delivery due to their special morphology and excellent surface properties. However, the preparation of the core–shell microspheres composed of hydroxyapatite (HA) have been rarely reported. In this paper, porous HA core–shell microspheres were prepared through a one-step hydrothermal method by using sodium trimetaphosphate (STMP) as the phosphorus source. SEM and TEM observations showed that the prepared porous HA core–shell microspheres were composed of a porous shell and a solid core, with a gap between the core and the shell. These microspheres bear uniform size and identical structure. With the increase of the hydrothermal time, the solid microspheres transformed to porous core–shell microspheres with the simultaneous transformation of their phase from amorphous calcium phosphate (ACP) to HA. The possible formation mechanism is proposed, providing inspiration for the design of porous HA core–shell microspheres and their potential biological applications.

© 2022 The Authors. Published by Elsevier B.V. This is an open access article under the CC BY-NC-ND license (<http://creativecommons.org/licenses/by-nc-nd/4.0/>).

**1. Introduction**

As the main inorganic component of natural bones and teeth, hydroxyapatite ( $\text{Ca}_{10}(\text{PO}_4)_6(\text{OH})_2$ ; HA) is one of the most widely studied calcium phosphates in biomedical field due to its excellent biocompatibility and bioactivity [1,2]. It is well known

that the morphology, composition and structure of HA have vital influences on its properties and further affect its applied efficacy [3–5]. Thus, various forms of HA including particles, rods, needles, fibers, sheets, tubes, and diverse microspheres being solid, porous, hollow and flower-like, have been prepared by various methods [6–8]. Among them, three-dimensional

\* Corresponding author.

E-mail address: [biosdu@sdu.edu.cn](mailto:biosdu@sdu.edu.cn) (Y.-p. Lu).

<https://doi.org/10.1016/j.jmrt.2022.01.001>

2238-7854/© 2022 The Authors. Published by Elsevier B.V. This is an open access article under the CC BY-NC-ND license (<http://creativecommons.org/licenses/by-nc-nd/4.0/>).

porous microspheres exhibit better selectivity for the separation and purification of bioactive macromolecules (such as proteins, nucleic acids, and biological enzymes) and high drug loading capacity [9,10]. Recently, core–shell particles with controlled structure and morphology have gradually been paid more attention due to their unique characteristics and potential applications in the field of drug delivery [11,12]. So the porous microsphere with core–shell structure is considered synthetically to achieve good fluidity, high specific surface area and tunable release kinetics. In addition, biodegradation properties are one of the most important features of drug carriers [13–15]. The long-term retention of drug carriers *in vivo* may bring potential toxicity risks. Core–shell structures have the potential to improve the degradability of HA carriers in physiological environments due to their rough and porous surfaces and gaps between the cores and the shells that allow adequate wetting of microspheres in solution [16].

The phase, structure and morphology of materials strongly depend on the synthetic methods and the parameters in the synthetic process [17–19]. Generally, HA microspheres can be obtained by hydrothermal method, spray drying method, sol–gel method, template method, solvothermal method and so on [20–22]. However, there are very few literature reports on the preparation of core–shell structured HA microspheres so far. Cho et al. [16] synthesized yolk–shell HA spheres with a diameter of 1–5 µm by spray drying in two steps. In the prior art, to obtain core–shell microspheres, it is usually necessary to coat the hydroxyapatite microspheres with a layer of polyelectrolyte, chitosan and other organic/inorganic molecules, or deposit a layer of hydroxyapatite on calcium carbonate, silica or other spherical substances [23–25]. So the facile preparation of pure HA microspheres with stable core–shell structure is still highly desirable and challenging.

Previous studies indicated that in normal mineralized tissues, the influence of phosphate on the precipitation of HA crystals is greater than that of calcium [26]. Sodium trimetaphosphate (STMP) is a phosphorylating agent commonly used in the food industry. It can react with the hydroxyl radical to introduce phosphate groups onto type I collagen surface and induce its mineralization. In addition, the presence of biomolecules such as amino acid can induce the nucleation of specific polymorph and influence the final unique morphology of crystals [27–29]. Accordingly, the selection of phosphorus sources and biomolecules plays a key role in fabricating the HA microspheres with specific structure.

Herein, we propose a one-step hydrothermal synthesis strategy of porous HA core–shell microspheres with STMP as the phosphorus source and L-glutamic acid as the additive. The evolution of the phase, morphology and microstructure of the core–shell structured HA microspheres with time gradient were investigated. The formation mechanism was discussed based on the evolutional information and TEM analysis.

## 2. Materials and method

### 2.1. Materials

Calcium nitrate tetrahydrate ( $\text{Ca}(\text{NO}_3)_2 \cdot 4\text{H}_2\text{O}$ , AR), sodium trimetaphosphate ( $(\text{NaPO}_3)_3$ , AR), nitric acid ( $\text{HNO}_3$ , AR), urea

$(\text{CO}(\text{NH}_2)_2$ ), and L-glutamic acid were purchased from Sino-pharm Chemical Reagent Co. Ltd. (Shanghai, China). All chemical reagents were used as received without any further purification.

### 2.2. Sample preparation

HA microspheres were prepared using a hydrothermal method. In a typical procedure, the aqueous solution of  $(\text{NaPO}_3)_3$  (0.02 mol/L, 100 mL) was added to  $\text{Ca}(\text{NO}_3)_2 \cdot 4\text{H}_2\text{O}$  solution (0.108 mol/L, 100 mL), followed by the addition of urea solution (1 mol/L, 50 mL), while the molar ratio of Ca/P was kept at 1.8. The initial pH values of the mixed solution were adjusted to 3.5 using dilute nitric acid solution ( $\text{HNO}_3$ ) of 0.5 mol/L under continuous magnetic stirring conditions. And then L-glutamic acid (0.015 mol) was added to the final solution. After being stirred for 20 min, the resulted mixture was transferred into a 300 mL Teflon-lined cylindrical stainless steel autoclave reactor, followed by hydrothermal treatment at 180 °C for 0.5, 1, 2, 4, 5, 10 and 15 h, respectively. After the reaction, the obtained precipitates were collected and washed thoroughly with deionized water and anhydrous ethanol to remove any excess ions and possible remnants, and finally freeze-dried to receive the final powder. In addition, the concentration gradient experiments of STMP were carried out when the hydrothermal time was maintained at 10 h and the corresponding concentrations of  $(\text{NaPO}_3)_3$  were 0.01 and 0.03 mol/L, respectively. The rest of the reaction conditions were consistent with the above experiment process.

### 2.3. Characterization

An X-ray diffractometer (XRD, EMPYREAN, 45 kV,  $\text{CuK}\alpha$  radiation,  $\lambda = 1.5404 \text{ \AA}$ ) and a Fourier transform infrared spectrometer (FTIR, NEXUS 670) were used to identify the phase and functional groups of the obtained samples. A field emission scanning electron microscope (FE-SEM, SU-70, 15 kV) was used to observe morphologies of samples, and examination of microstructures and selected area electron diffraction (SAED) of the samples were carried out on a high-resolution transmission electron microscope (HR-TEM, JEM-2100F, 200 kV). Before TEM observation, the product was dispersed ultrasonically in anhydrous ethanol for 30 min. A laser diffraction particle size analyzer (LS 13320) was used to measure the particle size distribution and mean particle size. Nitrogen adsorption–desorption isotherms were measured with a Micromeritics ASAP 2460 instrument.

## 3. Results and discussion

### 3.1. Phase analysis

XRD patterns and FT-IR spectra of the as-obtained samples for different hydrothermal times of 0.5, 1, 2, 4, 5, 10 and 15 h are shown in Fig. 1 to confirm the phase composition and functional groups. XRD patterns of the samples prepared at hydrothermal time of 0.5 and 1 h (Fig. 1A) show no obvious diffraction peaks and the diffused peak at about  $2\theta = 29^\circ$  indicates that these products are composed of amorphous

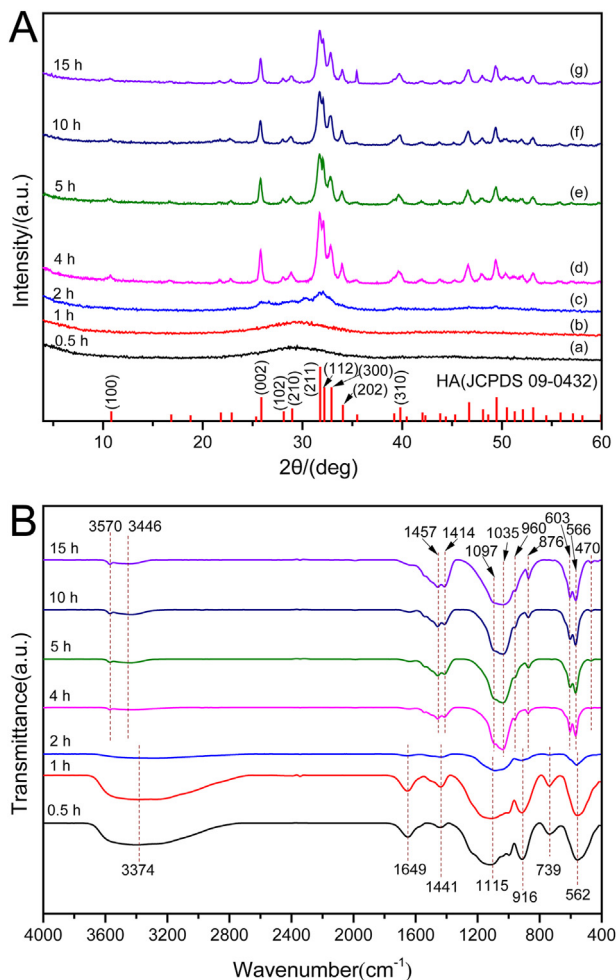


**Fig. 1 – XRD patterns (A) and FT-IR spectra (B) of the as-obtained samples hydrothermally synthesized for different hydrothermal times of 0.5 (a), 1 (b), 2 (c), 4 (d), 5 (e), 10 (f) and 15 h (g), respectively.**

calcium phosphate (ACP) phase. With the extension of hydrothermal time, the crystallinity gradually increases and all the diffraction peaks are well indexed to the standard diffraction data of HA (JCPDS card 09–0432). Particularly, when the hydrothermal time is 2 h, the diffraction peaks are broad and the peaks corresponding to the (211), (112) and (300) crystal planes overlap and show low peak intensity. According to the Debye–Scherer equation, it is revealed that the obtained HA has low crystallinity and fine crystallites [30]. The samples obtained under this condition contain a small amount of HA as well as ACP, which is due to the partial transformation from ACP to HA. When the hydrothermal time exceeds 2 h, pure HA with good crystallinity is obtained. The functional groups revealed by FT-IR spectra of the prepared samples further support the above phase evolution (Fig. 1B). The broad peaks at around 3446, 3374 and 1649  $\text{cm}^{-1}$  are ascribed to the  $\text{OH}^-$  group of water molecules. The single peak at 1441  $\text{cm}^{-1}$  is due to the characteristic vibration of  $\text{CO}_3^{2-}$ , which is produced by the hydrolysis of urea. The peaks at 1115 and 916  $\text{cm}^{-1}$  are attributed to the stretching vibration bands of P–O, and 562  $\text{cm}^{-1}$  is corresponding to bending vibration of

P–O, which are characteristics bands of  $\text{PO}_4^{3-}$ . The single peak at 562  $\text{cm}^{-1}$  illustrates that the products are amorphous calcium phosphate, while the anisotropic local electric field of crystalline apatite partially splits into an apparent doublet absorption band between 500 and 600  $\text{cm}^{-1}$ , and the broad absorption peak located at around 1115  $\text{cm}^{-1}$  is attributed to the characteristic vibration of ACP molecules [31]. When the hydrothermal time increases to 4 h and above, the products have similar patterns and the peak at around 3570  $\text{cm}^{-1}$  attributed to the stretching modes of  $\text{OH}^-$  in HA is detected indicating the integrity of the HA crystal structure. The broad and weak bimodal bands at 1457 and 1414  $\text{cm}^{-1}$ , and the peak at 876  $\text{cm}^{-1}$  are corresponding to the characteristic vibrations of  $\text{CO}_3^{2-}$  group, suggesting that the  $\text{CO}_3^{2-}$  group substitutes the B-site of  $\text{PO}_4^{3-}$  group in the HA. It is known that  $\text{CO}_3^{2-}$  is the common impurity to replace  $\text{PO}_4^{3-}$  in HA and will not produce adverse effects [32,33]. The peaks at around 1097, 1035, 960, 603, 566 and 470  $\text{cm}^{-1}$  are assigned to the  $\text{PO}_4^{3-}$  group in HA.

### 3.2. Microstructural characterization

The morphological and microstructural evolutions of the porous HA microspheres in a time-dependent approach, as characterized by FE-SEM and TEM, are shown in Figs. 2 and 3. Initially, smooth ACP microspheres (according to Fig. 1a) with a diameter of approximately 3–5  $\mu\text{m}$  are synthesized when the hydrothermal time is 0.5 h (Fig. 2a–c). Then, a small number of particles gradually appear on the surface of the microspheres. When the hydrothermal time is increased to 2 h, the surfaces of the microspheres become loose and there are particles attached to. As the hydrothermal time goes on, the particles gradually increase and accumulate to form a spherical shell with a gap to the inner core (Fig. 2k, n and q). Ultimately, the HA core–shell microspheres with a diameter of approximately 3–10  $\mu\text{m}$  are formed under the condition that the hydrothermal time is 10 h. The high magnification insert of the microsphere surface shows that the particles are orientationally assembled by nano whiskers to a dimension with a length of about 0.2–0.7  $\mu\text{m}$  and a width of about 0.1–0.3  $\mu\text{m}$  (Fig. 2r and u). It can be seen from the broken microspheres that the prepared HA core–shell microsphere consists of an inner core with a diameter of about 3–7  $\mu\text{m}$  and an outer shell with a thickness of about 0.3–0.8  $\mu\text{m}$ , and there exist gaps between the core and the shell (Fig. 2q, and t). When the time is prolonged to 15 h, the larger clusters lead to the tighter shell compared with the shorter hydrothermal times. In this process, the hydrothermal times of more than 4 h make the core–shell structure more complete and stable. At the same time, the products show good size uniformity under all hydrothermal conditions. In order to further investigate the influence of STMP amount on the microstructure of HA, different concentrations of STMP are introduced to the synthesis of HA microspheres when the hydrothermal time is 10 h. As shown in Fig. S1, the carbonated HA phases are obtained under the conditions of different concentrations of STMP, in which when the STMP concentration is 0.01 mol/L, a small amount of calcium carbonate is also produced. In addition, the morphologies of as-obtained products are inhomogeneous, which are mixtures of core–shell structure and solid spheres, regardless of whether the STMP concentration

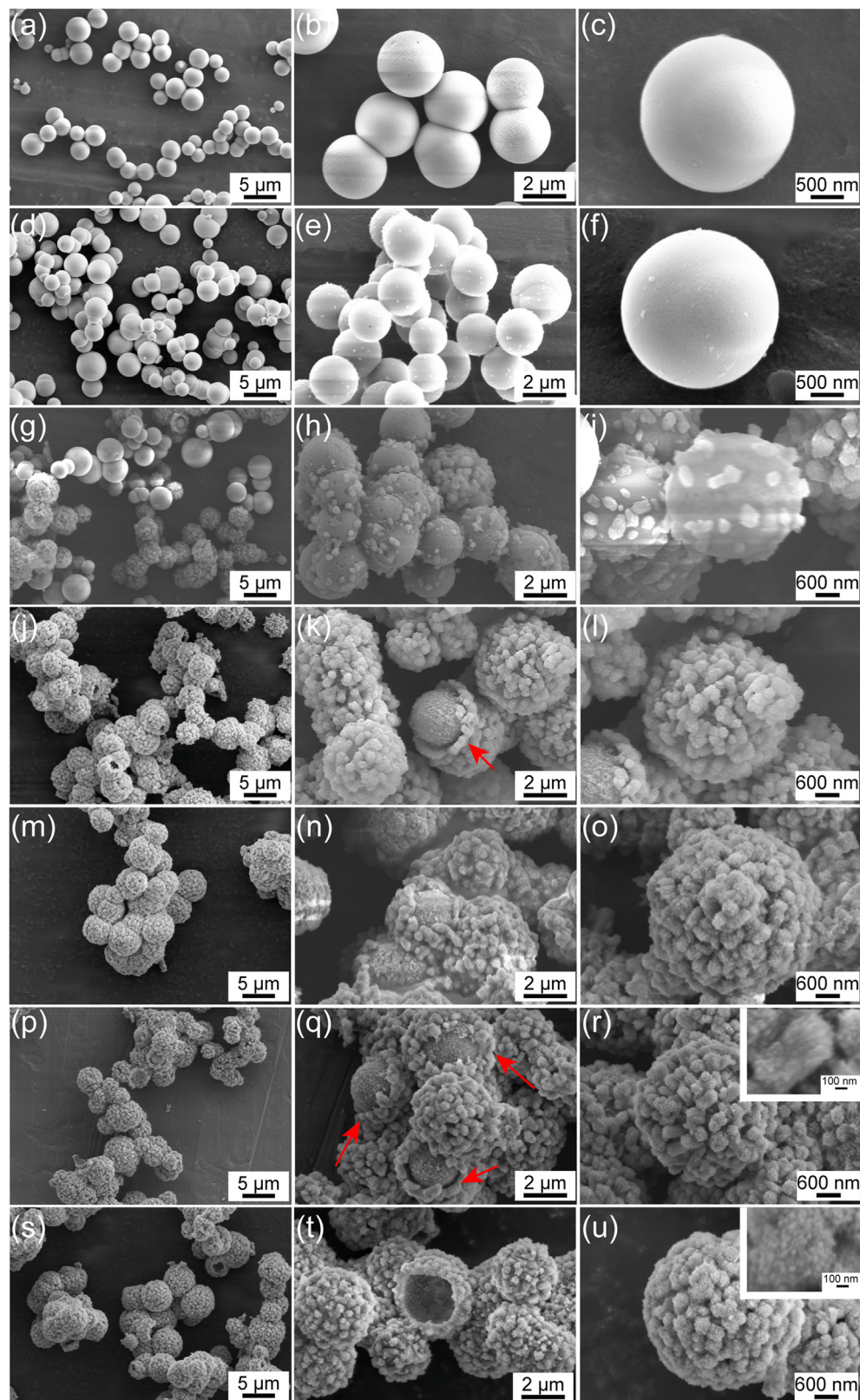
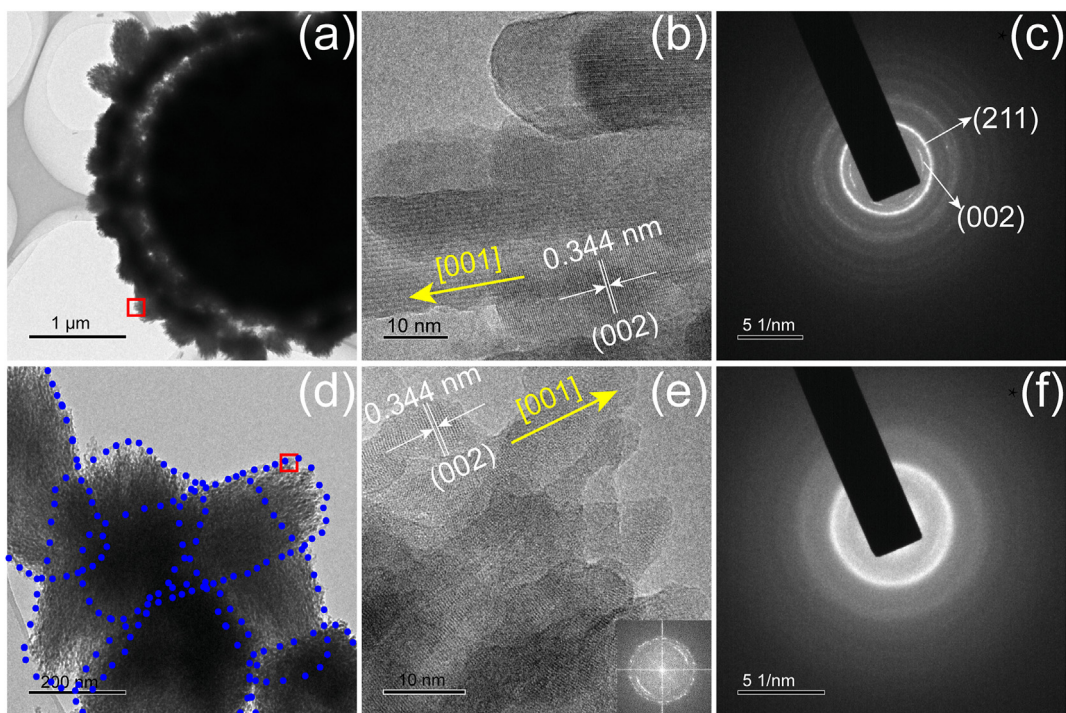


Fig. 2 – FE-SEM images of the as-obtained microspheres hydrothermal synthesized at 180 °C for different hydrothermal times of 0.5 (a–c), 1 (d–f), 2 (g–i), 4 (j–l), 5 (m–o), 10 (p–r) and 15 h (s–u), respectively.



**Fig. 3 – TEM images of the as-obtained powders at hydrothermal times for 10 h (a–c) and 2 h (d–f), respectively. Low magnifications (a) and (d), HR-TEM images (b) and (e) corresponding FFT pattern as an insert, and SAED patterns (c) and (f).**

is 0.01 or 0.03 mol/L. It can be explained by the reaction process of STMP in the hydrothermal system. When the STMP concentration is 0.01 mol/L, the saturation of  $P_3O_{10}^{5-}$  produced by the reaction of STMP and  $OH^-$  is correspondingly low, which affects the formation of the shell, so only part of the microspheres have the core–shell structure. When the STMP concentration is 0.03 mol/L, the extra  $P_3O_{10}^{5-}$  produced by the excess STMP can chelate with calcium ions, which hinder the aggregation of surrounding ions to lead to the inhomogeneous of the microspheres microstructures.

The HR-TEM and corresponding SAED analysis are performed to further investigated the phase and structure transformation of the microspheres (Fig. 3). The TEM image of the broken core–shell HA microspheres indicates that the shell of the microsphere is composed of connected particles, as well as a gap is formed between the shell and the core (Fig. 3a), which is consistent with SEM results. The HR-TEM image (Fig. 3b) of the particles on the surface of the microspheres (boxed in Fig. 3a) shows the lattice fringes with an interplanar spacing of 0.344 nm which corresponds to the (002) planes of HA. The SAED pattern (Fig. 3c) of the core part of the microspheres shows the diffraction rings which are

assigned to the diffractions of (211) and (002) planes of HA. Furthermore, it can be observed from Fig. 3d that the particles on the surface of the microspheres are composed of nano whiskers being about 0.2–0.7  $\mu$ m in length, which are consistent with the SEM observations of samples (Fig. 2r and u). The lattice fringes with an interplanar spacing of 0.344 nm correspond to the (002) planes of HA and the Fast Fourier Transform (FFT) insert further reveals the nano whiskers are crystalline HA and grow along preferred c-axis orientation (Fig. 3e). The diffuse diffraction ring present in the corresponding SAED pattern (Fig. 3f) indicates that the ACP and HA phases coexist.

### 3.3. Specific surface area and size distribution

The specific surface areas, pore volumes and mean pore sizes of the microspheres synthesized for different hydrothermal times of 1, 2, 4, 5 and 10 h are summarized in Table 1, in which sample ID are correspondingly named as T1, T2, T4, T5 and T10, respectively. The nitrogen adsorption–desorption isotherms, pore size distributions, particle size distributions and mean particle diameter histograms are shown in Fig. 4. When

**Table 1 – The characterization of the specific surface areas, pore volumes and mean pore sizes of the synthesized samples.**

Sample	BET surface area/ $m^2 \cdot g^{-1}$	Pore volume/ $cm^3 \cdot g^{-1}$	Mean pore size/nm
T1	1.0225	0.0198	8.1359
T2	13.1997	0.3481	9.5419
T4	42.7601	0.1432	12.0603
T5	49.2412	0.1496	10.7131
T10	47.8913	0.1650	13.0027

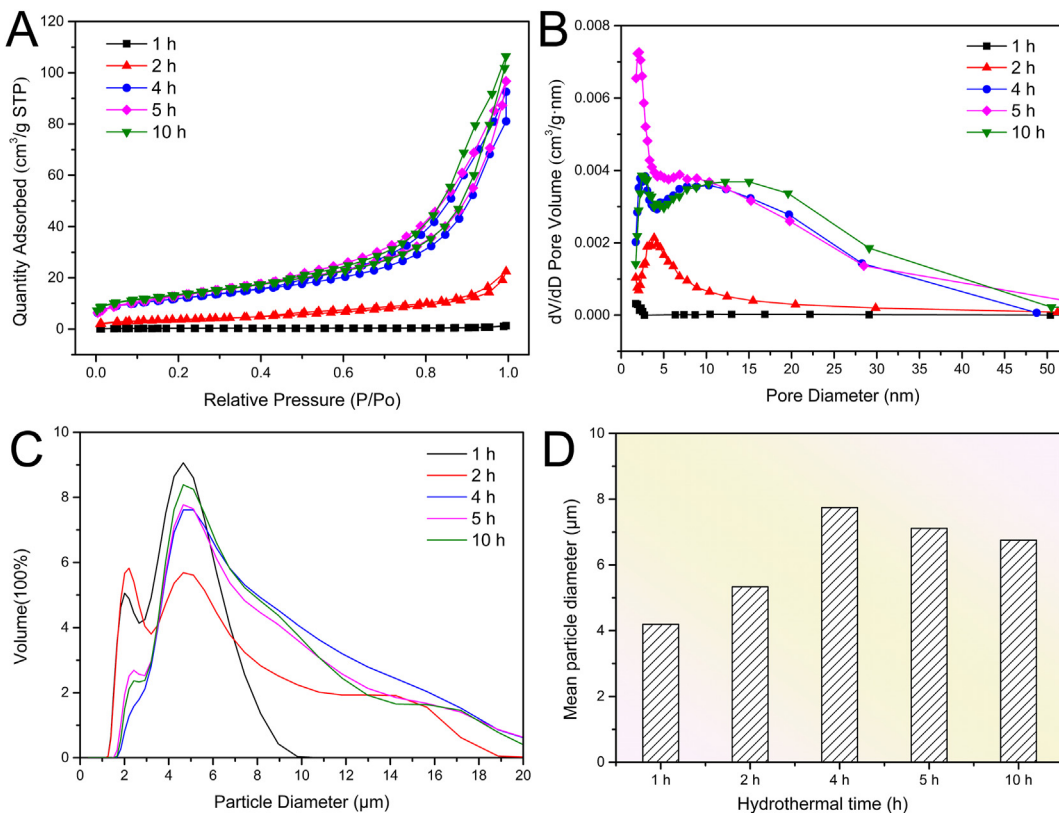


**Fig. 4 – Nitrogen adsorption–desorption isotherms (A), pore size distributions (B), particle size distributions (C) and mean particle diameter histograms (D) of the as-obtained powders for different hydrothermal times of 1, 2, 4, 5 and 10 h, respectively.**

the hydrothermal time is 1 h, the BET surface area of ACP shows a low number of  $1.0225 \text{ m}^2/\text{g}$ , which is due to the larger spherical associations of Posner's clusters and the apparent hindrance to nitrogen adsorption of these inner surfaces [34]. With the increase of the hydrothermal time, the specific surface area of the microspheres gradually increased to  $49.2412 \text{ m}^2/\text{g}$ . With the hydrothermal time exceeding 4 h, that is, after the formation of the core–shell structure, the specific surface area values of these microspheres are similar.

Accordingly, the nitrogen adsorption–desorption isotherms (Fig. 4A) show that the fabricated microspheres exhibit type IV isotherms with type H3 hysteresis loop attributed to the shell self-assembled by clusters with slit-shaped pores according to the IUPAC, indicating a typical mesoporous structure [35]. Similarly, the mean pore sizes of the microspheres increase with the hydrothermal time, and the pore diameter distributions are broader, meaning that more complex pore channels are conducive to the drug loading and sustained release. As

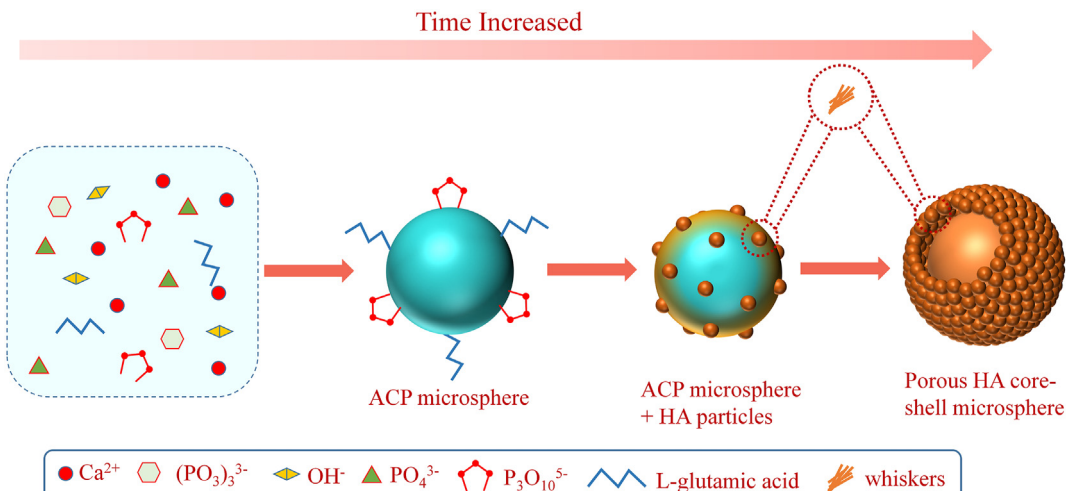
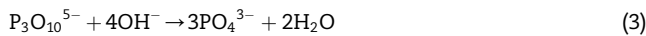
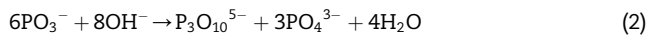


**Fig. 5 – Formation mechanism of porous HA core–shell microspheres by a one-step hydrothermal method.**

shown in Fig. 4C and D, the change of particle diameters from small to large corresponds to the transition of the microspheres from the solid ACP microspheres to the core–shell HA microspheres, as indicated by the prior SEM observations.

### 3.4. Formation mechanism of porous HA core–shell microspheres

It is definite that there happened the transformation from ACP microspheres to the nanocrystalline core–shell HA porous microspheres during the hydrothermal synthesis, with STMP as the phosphorous source. The relevant phase and structure evolutions are illustrated in Fig. 5. Hydrolysis of urea gradually produces OH<sup>−</sup> with the increase of hydrothermal time, which provides an alkaline environment for the reaction system based on the reaction Equation (1) [36]. Under alkaline conditions, the chemical changes of STMP in the hydrothermal system are shown as Equations (2) and (3) [37]. STMP reacts with OH<sup>−</sup> to generate P<sub>3</sub>O<sub>10</sub><sup>5−</sup> and PO<sub>4</sub><sup>3−</sup> firstly, and then the obtained P<sub>3</sub>O<sub>10</sub><sup>5−</sup> reacts with OH<sup>−</sup> to generate PO<sub>4</sub><sup>3−</sup> again.



When the Ca<sup>2+</sup> and PO<sub>4</sub><sup>3−</sup> in the solution are close to the supersaturation level, Ca–P clusters will be produced. The carboxyl group of glutamic acid can chelate with Ca<sup>2+</sup> in the solution to promote the aggregation of surrounding ions [38]. The charged side chain of glutamic acid is considered to be the main factor that promotes the formation and growth of Ca–P clusters, but does not enter the clusters [39]. The Posner's clusters with the chemical formula of Ca<sub>9</sub>(PO<sub>4</sub>)<sub>6</sub> are generally considered to be the basic units of ACP, and thus the key to apatite nucleation in solution [40,41]. Consequently, ACP microspheres are obtained at the beginning of the hydrothermal reaction due to their surface characteristics. At the same time, P<sub>3</sub>O<sub>10</sub><sup>5−</sup> can also chelate with Ca<sup>2+</sup> on the surface of ACP, and react with OH<sup>−</sup> to form PO<sub>4</sub><sup>3−</sup> as shown in the reaction Equation (3). Thus, active nucleation sites are formed on the surface of the ACP microspheres, and the whisker-like apatite nucleates, grows and self-assembles into nano clusters, following the dissolution–reprecipitation mechanism [42]. As the hydrothermal time prolonged, along with a small amount of dissolution of the internal microspheres surface, the external nano clusters gradually increase and accumulate to form a porous shell, which produce a gap to the internal microspheres. During the process, the internal ACP microspheres are transformed into HA crystals, which act as the final core. It is speculated that the phase transition of the internal microspheres may follow the surface-mediated transformation mechanism [43] and the reorganisation of Posner's clusters to build HA crystals [44]. The dissolution of the surface promotes ion migration, leading to the nucleation and growth of HA. In addition, the minimum activation energy is required for the simple reorganization of Posner's clusters to HA crystals in the inner core [45]. Finally, pure HA microspheres with core–shell structure are formed.

There are three key points in the whole process of preparing porous HA core–shell microspheres. Firstly, the slow hydrolysis of urea not only provides an alkaline environment for the nucleation and growth of HA, but also provides OH<sup>−</sup> for the hydrolysis of STMP. Under the action of urea, the hydrothermal reaction can proceed stably and continuously, ensuring the uniformity of the final crystal size. Secondly, glutamic acid acts as a surfactant to regulate the direction of crystals growth. The carboxyl group of glutamic acid can chelate with calcium ions on the HA crystal planes to form the soluble complex. Slow hydrolysis of the complex releases calcium ions to provide a sustained driving force for crystal growth [28]. Finally, the PO<sub>4</sub><sup>3−</sup> produced by the initial reaction of STMP with OH<sup>−</sup> acts as the phosphorus source for the formation of the core. The produced P<sub>3</sub>O<sub>10</sub><sup>5−</sup> binds to the calcium site on the surface of ACP to form the active site and improves the aggregation of other ions, which are conducive to the formation of the shell. Therefore, it is suggested that the gradual and multi-step reaction of raw materials is the key to the formation of porous HA core–shell microspheres. In the field of biological drug delivery, this porous HA core–shell microspheres may have great potential for high drug loading and slow drug release due to their special structure.

## 4. Conclusion

In summary, porous HA core–shell microspheres with an average diameter of about 7 μm are successfully prepared by using STMP as phosphorus source through a one-step hydrothermal method. The prepared porous HA core–shell microsphere consists of an inner core with a diameter of about 4–6 μm and an outer shell with a thickness of about 0.3–0.8 μm, and there is gap between the core and the shell. The time gradient experiment reveals the transition from the solid microspheres to the core–shell microspheres, and the corresponding phase transformation from ACP to HA. The as-obtained microspheres bear regular spherical morphology, uniform size distribution and high specific surface area. The possible formation mechanism is proposed based on the evolutionary information and TEM analysis. This study may provide a referential strategy to regulate the fine structure of HA microspheres, and the related biological performance and drug release behavior requires further studies.

## Declaration of Competing Interest

The authors declare that they have no known competing financial interests or personal relationships that could have appeared to influence the work reported in this paper.

## Acknowledgments

This work was supported by Natural Science Foundation of Shandong Province (ZR2017MEM014), National Natural Science Foundation of China (No. 52002223), Natural Science Foundation of Jiangsu Province (BK20190208). Thanks are due

to Shanghai Kindly Medical Instrument Co., Ltd. For financial support.

## Appendix A. Supplementary data

Supplementary data to this article can be found online at <https://doi.org/10.1016/j.jmrt.2022.01.001>.

## REFERENCES

- [1] Roy DM, Linnehan SK. Hydroxyapatite formed from coral skeletal carbonate by hydrothermal exchange. *Nature* 1974;247:220–2. <https://doi.org/10.1038/247220a0>.
- [2] Zhou H, Lee J. Nanoscale hydroxyapatite particles for bone tissue engineering. *Acta Biomater* 2011;7:2769–81. <https://doi.org/10.1016/j.actbio.2011.03.019>.
- [3] Goto T, Sasaki K. Synthesis of morphologically controlled hydroxyapatite from fish bone by urea-assisted hydrothermal treatment and its Sr<sup>2+</sup> sorption capacity. *Powder Technol* 2016;292:314–22. <https://doi.org/10.1016/j.powtec.2016.01.041>.
- [4] Ooi CH, Ling YP, Pung SY, Yeoh FY. Mesoporous hydroxyapatite derived from surfactant-templating system for p-Cresol adsorption: physicochemical properties, formation process and adsorption performance. *Powder Technol* 2019;342:725–34. <https://doi.org/10.1016/j.powtec.2018.10.043>.
- [5] Ahmed MK, Ramadan R, Afifi M, Menazea AA. Au-doped carbonated hydroxyapatite sputtered on alumina scaffolds via pulsed laser deposition for biomedical applications. *J Mater Res Technol* 2020;9:8854–66. <https://doi.org/10.1016/j.jmrt.2020.06.006>.
- [6] Sadat-Shojaei M, Khorasani MT, Dinpanah-Khoshdargi E, Jamshidi A. Synthesis methods for nanosized hydroxyapatite with diverse structures. *Acta Biomater* 2013;9:7591–621. <https://doi.org/10.1016/j.actbio.2013.04.012>.
- [7] Guo YJ, Wang YY, Chen T, Wei YT, Chu LF, Guo YP. Hollow carbonated hydroxyapatite microspheres with mesoporous structure: hydrothermal fabrication and drug delivery property. *Mater Sci Eng C* 2013;33:3166–72. <https://doi.org/10.1016/j.msec.2013.03.040>.
- [8] Huang A, Dai H, Wu X, Zhao Z, Wu Y. Synthesis and characterization of mesoporous hydroxyapatite powder by microemulsion technique. *J Mater Res Technol* 2019;8:3158–66. <https://doi.org/10.1016/j.jmrt.2019.02.025>.
- [9] Kong X, Xu S, Wang X, Cui F, Yao J. Calcium carbonate microparticles used as a gene vector for delivering p53 gene into cancer cells. *J Biomed Mater Res* 2012;100:2312–8. <https://doi.org/10.1002/jbm.a.34155>.
- [10] Zhang C, Shan S, Hu T, Wang G, Zhi Y, Su H, et al. Recent progress on biomedical applications of functionalized hollow hydroxyapatite microspheres. *Ceram Int* 2021;47:13552–71. <https://doi.org/10.1016/j.ceramint.2021.01.214>.
- [11] Su H, Tian Q, Hurd Price CA, Xu L, Qian K, Liu J. Nanoporous core@shell particles: design, preparation, applications in bioadsorption and biocatalysis. *Nano Today* 2020;31:100834. <https://doi.org/10.1016/j.nantod.2019.100834>.
- [12] Ahmed MK, Al-Wafi R, Mansour SF, El-dek SI, Uskoković V. Physical and biological changes associated with the doping of carbonated hydroxyapatite/polycaprolactone core-shell nanofibers dually, with rubidium and selenite. *J Mater Res Technol* 2020;9:3710–23. <https://doi.org/10.1016/j.jmrt.2020.01.108>.
- [13] Lu Y, Hu Q, Lin Y, Pacardo DB, Wang C, Sun W, et al. Transformable liquid-metal nanomedicine. *Nat Commun* 2015;6:10066. <https://doi.org/10.1038/ncomms10066>.
- [14] Torresan V, Forrer D, Guadagnini A, Badocco D, Pastore P, Casarin M, et al. 4D multimodal nanomedicines made of nonequilibrium Au-Fe alloy nanoparticles. *ACS Nano* 2020;14:12840–53. <https://doi.org/10.1021/acsnano.0c03614>.
- [15] Liu Y, Tang Y, Wu J, Sun J, Liao X, Teng Z, et al. Facile synthesis of biodegradable flower-like hydroxyapatite for drug and gene delivery. *J Colloid Interface Sci* 2020;570:402–10. <https://doi.org/10.1016/j.jcis.2020.03.010>.
- [16] Cho JS, Chan Kang Y. Advanced yolk–shell hydroxyapatite for bone graft materials: kilogram-scale production and structure-in vitro bioactivity relationship. *RSC Adv* 2014;4:25234. <https://doi.org/10.1039/c4ra02925a>.
- [17] Lin K, Liu P, Wei L, Zou Z, Zhang W, Qian Y, et al. Strontium substituted hydroxyapatite porous microspheres: surfactant-free hydrothermal synthesis, enhanced biological response and sustained drug release. *Chem Eng J* 2013;222:49–59. <https://doi.org/10.1016/j.cej.2013.02.037>.
- [18] Lin K, Wu C, Chang J. Advances in synthesis of calcium phosphate crystals with controlled size and shape. *Acta Biomater* 2014;10:4071–102. <https://doi.org/10.1016/j.actbio.2014.06.017>.
- [19] Xiao W, Gao H, Qu M, Liu X, Zhang J, Li H, et al. Rapid microwave synthesis of hydroxyapatite phosphate microspheres with hierarchical porous structure. *Ceram Int* 2018;44:6144–51. <https://doi.org/10.1016/j.ceramint.2017.12.247>.
- [20] Jiao Y, Lu YP, Xiao GY, Xu WH, Zhu RF. Preparation and characterization of hollow hydroxyapatite microspheres by the centrifugal spray drying method. *Powder Technol* 2012;217:581–4. <https://doi.org/10.1016/j.powtec.2011.11.025>.
- [21] Qi ML, Qi J, Xiao GY, Zhang KY, Lu CY, Lu YP. One-step hydrothermal synthesis of carbonated hydroxyapatite porous microspheres with a large and uniform size regulated by L-glutamic acid. *CrystEngComm* 2016;18:5876–84. <https://doi.org/10.1039/c6ce00902f>.
- [22] Wang YC, Xu WL, Lu YP, Xu WH, Yin H, Xiao GY. Investigation of nature of starting materials on the construction of hydroxyapatite 1D/3D morphologies. *Mater Sci Eng C* 2020;108:110408. <https://doi.org/10.1016/j.msec.2019.110408>.
- [23] Wang Y, Hassan MS, Gunawan P, Lau R, Wang X, Xu R. Polyelectrolyte mediated formation of hydroxyapatite microspheres of controlled size and hierarchical structure. *J Colloid Interface Sci* 2009;339:69–77. <https://doi.org/10.1016/j.jcis.2009.07.023>.
- [24] Teng SH, Wang P. One-pot synthesis of HA-coated gelatin microspheres by an emulsion method. *Mater Lett* 2011;65:1348–50. <https://doi.org/10.1016/j.matlet.2011.01.079>.
- [25] Zhao H, Tang J, Zhou D, Weng Y, Qin W, Liu C, et al. Electrospun icariin-loaded core-shell collagen, polycaprolactone, hydroxyapatite composite scaffolds for the repair of rabbit tibia bone defects. *Int J Nanomed* 2020;15:3039–56. <https://doi.org/10.2147/IJN.S238800>.
- [26] Jiang SD, Yao QZ, Ma YF, Zhou GT, Fu SQ. Phosphate-dependent morphological evolution of hydroxyapatite and implication for biominerallisation. *Gondwana Res* 2015;28:858–68. <https://doi.org/10.1016/j.gr.2014.04.005>.
- [27] Wang Z, Xu Z, Zhao W, Sahai N. A potential mechanism for amino acid-controlled crystal growth of hydroxyapatite. *J Mater Chem B* 2015;3:9157–67. <https://doi.org/10.1039/c5tb01036e>.
- [28] Tavafoghi M, Cerruti M. The role of amino acids in hydroxyapatite mineralization. *J R Soc Interface* 2016;13. <https://doi.org/10.1098/rsif.2016.0462>.

- [29] Li Z, Ren Q, Cui J, Hu D, Tian T, He T, et al. Comparing the efficacy of hydroxyapatite nucleation regulated by amino acids, poly-amino acids and an amelogenin-derived peptide. *CrystEngComm* 2020;22:3814–23. <https://doi.org/10.1039/c9ce01925a>.
- [30] Holzwarth U, Gibson N. The Scherrer equation versus the 'Debye-Scherrer equation'. *Nat Nanotechnol* 2011;6:534. <https://doi.org/10.1038/nnano.2011.145>.
- [31] Gadaleta SJ, Paschalidis EP, Betts F, Mendelsohn R, Boskey AL. Fourier transform infrared spectroscopy of the solution-mediated conversion of amorphous calcium phosphate to hydroxyapatite: new correlations between X-ray diffraction and infrared data. *Calcif Tissue Int* 1996;58:9–16. <https://doi.org/10.1007/BF02509540>.
- [32] Vignoles M, Bonel G, Holcomb DW, Young RA. Influence of preparation conditions on the composition of type B carbonated hydroxyapatite and on the localization of the carbonate ions. *Calcif Tissue Int* 1988;43:33–40. <https://doi.org/10.1007/BF02555165>.
- [33] Zhong Q, Li W, Su X, Li G, Zhou Y, Kundu SC, et al. Degradation pattern of porous CaCO<sub>3</sub> and hydroxyapatite microspheres in vitro and in vivo for potential application in bone tissue engineering. *Colloids Surf B Biointerfaces* 2016;143:56–63. <https://doi.org/10.1016/j.colsurfb.2016.03.020>.
- [34] Holmes JM, Beebe RA. Surface areas by gas adsorption on amorphous calcium phosphate and crystalline hydroxyapatite. *Calcif Tissue Res* 1971;7:163–74. <https://doi.org/10.1007/BF02062604>.
- [35] Kruk M, Jaroniec M. Gas adsorption characterization of ordered organic-inorganic nanocomposite materials. *Chem Mater* 2001;13:3169–83. <https://doi.org/10.1021/cm0101069>.
- [36] Parthiban SP, Kim IY, Kikuta K, Ohtsuki C. Effect of urea on formation of hydroxyapatite through double-step hydrothermal processing. *Mater Sci Eng C* 2011;31:1383–8. <https://doi.org/10.1016/j.msec.2011.05.005>.
- [37] Zhang YG, Zhu YJ, Chen F, Sun TW. Biocompatible, ultralight, strong hydroxyapatite networks based on hydroxyapatite microtubes with excellent permeability and ultralow thermal conductivity. *ACS Appl Mater Interfaces* 2017;9:7918–28. <https://doi.org/10.1021/acsmami.6b13328>.
- [38] Wang W, Xue Z, Wang R, Wang X, Xu D. Molecular dynamics exploration of the growth mechanism of hydroxyapatite nanoparticles regulated by glutamic acid. *J Phys Chem B* 2021;125:5078–88. <https://doi.org/10.1021/acs.jpcb.1c02447>.
- [39] Xue Z, Yang M, Xu D. Nucleation of biomimetic hydroxyapatite nanoparticles on the surface of type I collagen: molecular dynamics investigations. *J Phys Chem C* 2019;123:2533–43. <https://doi.org/10.1021/acs.jpcc.8b10342>.
- [40] Posner AS, Betts F. Synthetic amorphous calcium-phosphate and its relation to bone-mineral structure. *Accounts Chem Res* 1975;8:273–81. <https://doi.org/10.1021/Ar50092a003>.
- [41] Swift MW, Van de Walle CG, Fisher MPA. Posner molecules: from atomic structure to nuclear spins. *Phys Chem Chem Phys : Phys Chem Chem Phys* 2018;20:12373–80. <https://doi.org/10.1039/c7cp07720c>.
- [42] Eanes ED. Amorphous calcium phosphate. *Monogr Oral Sci* 2001;18:130–47. <https://doi.org/10.1159/000061652>.
- [43] Tao J, Pan H, Wang J, Wu J, Wang B, Xu X, et al. Evolution of amorphous calcium phosphate to hydroxyapatite probed by gold nanoparticles. *J Phys Chem C* 2008;112:14929–33. <https://doi.org/10.1021/jp804371u>.
- [44] Abbona F, Baronnet A. A XRD and TEM study on the transformation of amorphous calcium phosphate in the presence of magnesium. *J Cryst Growth* 1996;165:98–105. [https://doi.org/10.1016/0022-0248\(96\)00156-X](https://doi.org/10.1016/0022-0248(96)00156-X).
- [45] Onuma K. Recent research on pseudobiological hydroxyapatite crystal growth and phase transition mechanisms. *Prog Cryst Growth Char Mater* 2006;52:223–45. <https://doi.org/10.1016/j.pcrystgrow.2006.06.003>.